Journal of Non-Newtonian Fluid Mechanics 264 (2019) 48–61

Contents lists available at ScienceDirect

Journal of Non-Newtonian Fluid Mechanics

journal homepage: www.elsevier.com/locate/jnnfm

Proper Orthogonal Decomposition (POD) of the flow dynamics for a viscoelastic fluid in a four-roll mill geometry at the Stokes limit

Paloma Gutierrez-Castillo*, Becca Thomases

Department of Mathematics, University of California, Davis, CA 95616, USA

ARTICLE INFO

Keywords:
Viscoelastic fluids
POD
Oldroyd-B

ABSTRACT

Numerical simulations of viscoelastic fluids in the Stokes limit with a four-roll mill background force were performed at a range of Weissenberg number (non-dimensional relaxation time). For small Weissenberg number the flow is steady and symmetric but upon increasing the Weissenberg number (corresponding to increased elasticity or flow memory time), the flow becomes unstable leading to a variety of temporal evolutions to different periodic and aperiodic solutions. These dynamics were analyzed using a Proper Orthogonal Decomposition (POD) that extracted elastic modes in terms of their contribution to the energy of the system. The temporal behavior of the system, captured by the decomposition, indicates that the motion of the stagnation points drives the different flow transitions. In particular, a transition to an asymmetric state occurs when the extensional stagnation points lose their pinning to the background forcing. A further transition to higher frequency modal dynamics occurs when the stagnation points that were initially tied by the forcing to the centers of the rolls, begin to move. The relative frequencies of the motion of these stagnation points is a critical factor in determining the complexity of the flow, measured by the number of modes needed to capture most of the energy in the system. Even when the flows are more complex a small number of modes is sufficient to capture the time evolution of these flows, demonstrating the usefulness of the POD applied to viscoelastic fluids at zero Reynolds number.

1. Introduction

Instabilities in viscoelastic fluids in the low Reynolds number regime, where viscous effects dominate inertia, have been studied for many years; see [1–10]. These instabilities are connected to increased flow resistance [11], the creation of secondary vortex flows [12], and can lead to a flow state referred to as “elastic turbulence” [13–16]. Instabilities and turbulence in low Reynolds number viscoelastic fluids also can yield high levels of mixing which is typically difficult to achieve in micro-fluidics or at low velocities [17].

Numerical simulations have proven to be a useful tool to study elastic instabilities [16,18–25], with both the cross-slot and the 4-roll mill geometry allowing the study of the onset of complex dynamics near steady extensional points. There has been some theoretical work regarding transitions to turbulence and criteria for instabilities, [5,26,27]. However, there is much left to understand regarding the development of “elastic turbulence”, and the nature of the flows in these high Weissenberg number (or long relaxation time) low Reynolds number fluids.

Nearly singular solutions in the Oldroyd-B model of a viscoelastic fluid were identified in [19] at extensional points in a flow with a simple four-roll mill background force. It was shown that the polymer stress concentrates into thin “stress islands” that are symmetric along the axis of extension. Beyond a critical Weissenberg number (Wi) the polymer stress grows exponentially in time (or faster) at the extensional point. With some numerical regularization it was shown that complex dynamics emerge beyond a critical Wi when the flow is highly stretched at the extensional point [23,24]. There are two transitions upon increasing Wi, first to an asymmetric state, and second to time-dependence. The transitions are similar to those identified in experiments [9] at an extensional point in a cross-slot flow. Experiments that are closer to the 4-roll mill periodic geometry of the simulations were done in [28] where a 4x4 checkerboard of rotating disks drives a flow of a thin layer of a dilute polymer solution. In this experiment a transition to asymmetry was found for a critical Wi, next they observe a three dimensional instability driving the free surface to buckle but for sufficiently large Wi the flow does become oscillatory. Simulations also uncovered interesting dynamics with the same numerical set-up from [23,24] using an alternate method to find periodic solutions [29] and a bifurcation diagram was mapped out locally around that solution.

Here we will introduce a Proper Orthogonal Decomposition (POD) of numerical solutions to the Oldroyd-B model for viscoelastic fluids at zero Reynolds number. POD has been a useful tool for analyzing instabilities and turbulent flows in Newtonian fluid dynamics for many years, see for example [30–37]. The review [37] gives a thorough overview of

* Corresponding author.
E-mail addresses: pgutierrez@math.ucdavis.edu (P. Gutierrez-Castillo), bthomases@math.ucdavis.edu (B. Thomases).

https://doi.org/10.1016/j.jnnfm.2018.12.009
Received 6 September 2018; Received in revised form 18 December 2018; Accepted 21 December 2018
Available online 22 December 2018
0377-0257/

modal decomposition with particular applications to fluid mechanics. Despite the frequent use of POD for Newtonian fluid dynamics, the only application to the Oldroyd-B model appeared in [38] to analyze viscoelastic fluids in the high Reynolds number regime. A difficulty with applying the techniques of POD to complex fluids arises because there is no natural inner-product space on the set of symmetric, positive definite tensors, and the elastic energy in the system (for the Oldroyd-B model) comes from the integral of the trace of the conformation tensor [39]. This is addressed in [38] by defining a POD on the unique symmetric square-root of the elastic stress tensor, and we employ this technique here as well. Another method to decompose the conformation tensor was recently introduced in [40] as a method to study turbulence in viscoelastic fluids.

In what follows we will first describe the numerical framework for our exploration, including an introduction to the POD for viscoelastic fluids at zero Reynolds number. The main part of the paper describes the results of the viscoelastic POD for the Oldroyd-B model at zero Reynolds number. We also describe some results obtained using the FENE-P model [41], a macroscopic closure that enforces finite extension of polymeric coils at the micro-scale.

2. Model

We use the Oldroyd-B model of a viscoelastic fluid at low Reynolds number, with explicit polymer stress diffusion, given in dimensionless form by

$$\Delta \mathbf{u} - \nabla p + \beta \nabla \cdot \mathbf{S} = \mathbf{f}, \tag{1}$$

$$\nabla \cdot \mathbf{u} = 0 \tag{2}$$

$$\partial_t \mathbf{S} + \mathbf{u} \cdot \nabla \mathbf{S} - \left(\nabla \mathbf{u} \mathbf{S} + \mathbf{S} \nabla \mathbf{u}^T\right) + \mathrm{Wi}^{-1}(\mathbf{I} - \mathbf{S}) = \nu_p \Delta \mathbf{S}, \tag{3}$$

for $\mathbf{u}$ the fluid velocity, p the fluid pressure, and $\mathbf{S}$, the (symmetric) conformation tensor, a macroscopic average of the polymer orientation and stretching that is related to the polymer stress tensor by $\boldsymbol{\tau}_p = \beta(\mathbf{S} - \mathbf{I})$. The parameters, β, the non-dimensional polymer stiffness, and Wi, the Weissenberg number, or non-dimensional relaxation time, are defined by

$$\beta = \frac{GL}{\mu U}, \quad \mathrm{Wi} = \frac{\lambda U}{L}, \tag{4}$$

for μ the solvent viscosity, λ the fluid relaxation time, G the polymer elastic modulus, L the system size, and U a characteristic velocity scale. Note that the Oldroyd-B model has $\nu_p = 0$ in Eq. (3). The polymer stress diffusion term, $\nu_p \Delta \mathbf{S}$, for ν_p small, is included in the right-hand side of Eq. (3) as a numerical regularization, and this modification to the Oldroyd-B model will be described in detail in the next section.

The background force is given by:

$$\mathbf{f} = \begin{pmatrix} 2 \sin x \cos y \\ -2 \cos x \sin y \end{pmatrix}, \tag{5}$$

which in a Newtonian Stokes flow ($\beta = 0$) corresponds to a four-roll velocity field $\mathbf{u} = -\frac{1}{2}\mathbf{f}$. The Stokes solution sets the characteristic (inverse) time scale $U/L = 1$.

2.1. Numerical details and parameters

The system Eqs. (1)–(3) are solved in a 2D periodic domain, $[0, 2\pi)^2$ with $N = 256$ grid points in each direction, giving $dx \approx 0.025$. We use a spectral method to solve the Stokes equations and time-step the advection equation for the conformation tensor in Fourier space using a second order Adams–Bashforth method with time step $dt = 0.0025$. This is the same numerical set-up used in [23,24] where the flow transitions that are discussed here were first observed. Some of the dynamics in this problem occur on very long time-scales and to capture the slow dynamics we run our simulations until at least $t = 1200\mathrm{Wi}$, and in some cases longer. To compute the solutions we start from a random perturbation of the low Fourier modes from isotropic initial polymer stress $\mathbf{S} = \mathbf{I}$. A similar approach was used in [24], but in this study the same random initial condition was used for all the simulations.

The quantity $\beta \cdot \mathrm{Wi}$ is the ratio of the polymer viscosity to solvent viscosity, so that given a particular working fluid the ratio is fixed independently of experimental conditions. In our simulations $\beta \cdot \mathrm{Wi} = 0.5$ is fixed. This value is consistent with the fluids used in experiments of dilute polymer solutions with highly viscous solvents, Boger fluids, (see, for example, [9]).

It is known that the Oldroyd-B model with the four-roll mill forcing has numerical difficulties associated with the lack of scale dependent diffusion and without adding some numerical regularization Eq. (1)–(3) (with $\nu_p = 0$) will form a singularity (perhaps at infinite time) [19,42,43]. Therefore, we include scale dependent polymer stress diffusion to the right-hand side of Eq. (3), of the form $\nu_p = c(dx^2)$ and $c = 1.66$. Scale dependent polymer diffusion will regularize the solutions so that long-time solutions are smooth [44] and upon grid refinement the solutions converge to the Oldroyd-B model. Analytically it has been shown that global solutions to the Stokes–Oldroyd-B model with diffusion exist for any $c > 0$ [45], but for $c = 0$, this is still an open question even in 2D.

2.2. Viscoelastic proper orthogonal decomposition

The main tool we employ to analyze the solutions from our simulations is the Proper Orthogonal Decomposition (POD), also known as the Karhunen–Loève analysis, or principal component analysis. This method provides an algorithm to decompose a set of data into a minimal number of basis functions or modes to capture as much energy as possible. Furthermore, the obtained modes are ordered in terms of the percent of energy contained in each mode.

See [33,37] for a review of decomposition methods in fluid dynamics, and [38] for an application of this method to viscoelastic flows at non-zero Reynolds number. To our knowledge this is the first application of a POD analysis of a viscoelastic flow at zero Reynolds number. We sketch the algorithm below and set up the notation for what follows.

We consider the POD for a vector $\mathbf{q}(\boldsymbol{\xi}, t) \in \mathbb{R}^n$ that is a function of spatial variables $\boldsymbol{\xi}$, and time t. In our application we will assume a separation of space and time and look for a decomposition around the temporal mean, $\bar{\mathbf{q}}$, of the form

$$\mathbf{q}(\boldsymbol{\xi}, t) - \bar{\mathbf{q}}(\boldsymbol{\xi}) = \sum_j a_j(t) \boldsymbol{\phi}_j(\boldsymbol{\xi}), \tag{6}$$

where $a_j(t)$ are the (scalar) temporal coefficients and $\boldsymbol{\phi}_j(\boldsymbol{\xi})$ are the spatial or geometric modes. To compute any POD, we consider a time-interval $t \in t_0 - t_{\mathrm{end}}$ in equally spaced time increments Δt. In what follows we will give the time-interval and increments that we use in each POD (note it is not necessary to use the same grid refinement or time-resolution for the POD as the original simulation). The vector we decompose is the unique symmetric square-root, $\mathbf{b}$, of the symmetric conformation tensor $\mathbf{S} = \mathbf{b}^2$, this choice is made so that the energy in the system can be written in terms of the stored elastic energy, as will be explained further below. To give an ordering for $\mathbf{b}$ as a vector we write

$$q_j(\boldsymbol{\xi}, t) = \begin{bmatrix} (b_{11})_j(x, y, t) \\ (b_{12})_j(x, y, t) \\ (b_{22})_j(x, y, t) \end{bmatrix}, \tag{7}$$

for $j = 1, \ldots, N_t$, where N_t is the number of snapshots of the data to include, defined below.

We employ the method of snapshots over a time-interval $t \in t_0 - t_{\mathrm{end}}$ because often the number of snapshots of data needed to resolve the temporal behavior $N_t = \frac{t_{end} - t_0}{\Delta t}$ is far less than the number of spatial variables $n = 3N^2$, i.e. $N_t << n$.

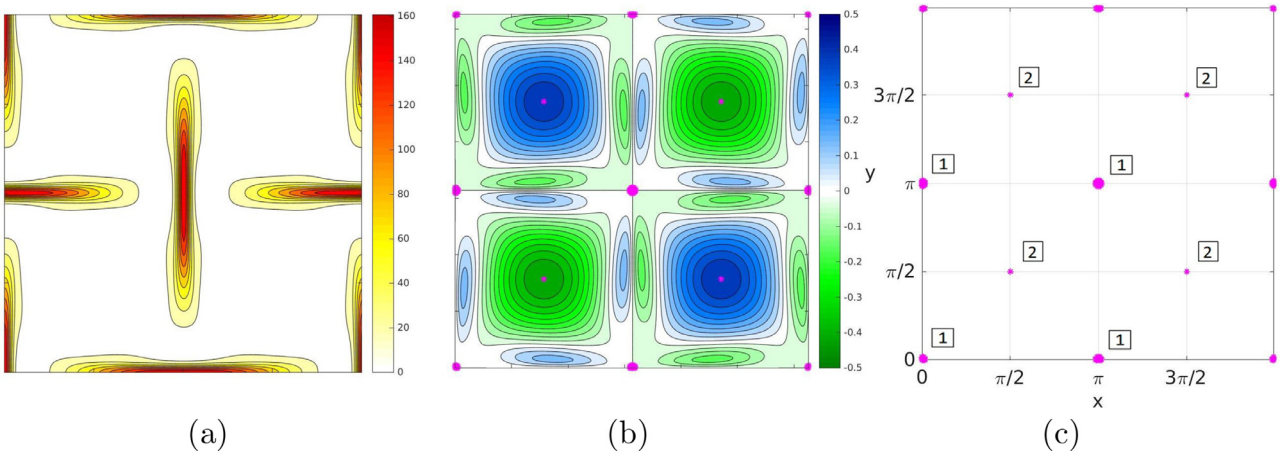

Fig. 1. Solution for Wi = 5 at t=6000 (a) Contours of tr**S**, (b) Vorticity contours, and (c) Stagnation points of vector field with threshold of 10^{-4}.

The POD is based on an eigenfunction decomposition of the system in the form

$$X^T X \boldsymbol{\psi}_j = E_j \boldsymbol{\psi}_j, \text{ for } \boldsymbol{\psi} \in \mathbb{R}^{N_t},$$

where

$$X = \left[\mathbf{x}(t_1)\, \mathbf{x}(t_2) \ldots \mathbf{x}(N_t)\right] \in \mathbb{R}^{n \times N_t},$$

and $\mathbf{x} = \mathbf{q} - \bar{\mathbf{q}}$. The geometric modes are recovered from the $\boldsymbol{\psi}$ via

$$\boldsymbol{\phi}_j = X \boldsymbol{\psi}_j \frac{1}{\sqrt{E_j}}, \text{ for } j = 1, \ldots . N_t.$$

The eigenvalues E_j represent how much of the original data is captured by each mode. The temporal coefficients are reconstructed by

$$a_j(t) = \left(\mathbf{q}(\boldsymbol{\xi}, t) - \bar{\mathbf{q}}(\boldsymbol{\xi}), \boldsymbol{\phi}_j(\boldsymbol{\xi})\right)_E,$$

where $(,)_E$ is the inner-product defining the energy space.

Ordering the modes by the size of E_j, we can retain modes that capture as much of the original data (in an L^2 sense) as we like. In what follows we keep the number of modes to capture at least 95% of the original data, i.e. we keep $r << N_t$ modes such that

$$\sum_{j=1}^{r} E_j / \sum_{j=1}^{N_t} E_j > 0.95.$$

In terms of compression of data this can be a significant savings, for example in what follows we find that $r = 14$ is the largest number of modes we need to keep to capture 95% of the energy in all the cases we consider.

In fluid dynamics this technique is useful because if we choose $\mathbf{q} = \mathbf{u}$ to be the velocity of the fluid, then the relevant vector space has inner product

$$(\mathbf{u}, \mathbf{v})_E = \frac{1}{V} \int_V \frac{1}{2} \rho \mathbf{u} \cdot \mathbf{v} dx$$

and the kinetic energy per unit volume is

$$\mathbf{E} = \frac{1}{V} \int_V \frac{1}{2} \rho |\mathbf{u}|^2 \, dx = (\mathbf{u}, \mathbf{u})_E \tag{8}$$

In this case the eigenvalues will represent how much kinetic energy fluctuations in the system is captured by each mode. In a viscoelastic fluid modeled by the Oldroyd-B equations the conformation tensor represents the amount of stored elastic energy in a volume of fluid [41], via

$$\mathbf{E}_{\text{ve}} = \frac{1}{V} \int_V \frac{1}{2} \beta \text{tr} \mathbf{S} dx.$$

This energy does not have a natural representation as an inner-product, in part because the set of symmetric positive definite matrices is not a vector-space [39]. However if we write $\mathbf{S}$ in terms of the unique symmetric square-root [46], $\mathbf{S} = \mathbf{b}^2$ or $S_{ij} = b_{ik} b_{kj}$, then we can see that $\text{tr}\mathbf{S} = \text{tr}(\mathbf{b}^2) = b_{ij}^2$. Thus if we introduce the inner product

$$\left(\mathbf{b}, \mathbf{b}'\right)_{\text{ve}} = \frac{1}{V} \int_V \frac{1}{2} \beta \, b_{ij} b'_{ij} \, dV, \tag{9}$$

we have $\mathbf{E}_{\text{ve}} = (\mathbf{b}, \mathbf{b})_{\text{ve}}$. A POD using this inner product will lead to eigenvalues that measure fluctuations in the stored elastic energy per unit volume. In the case of the Oldroyd-B model this energy is the mechanical energy, and although this is not strictly true for other models (such as FENE-P) this energy still gives a POD formulation of other systems.

For each Wi, we will compute a POD as described above on some specified temporal domain $t \in [t_0 - t_{\text{end}}]$ with a given Δt. We will retain the minimum number of modes to capture 95%$\mathbf{E}_{\text{ve}}$. The POD will give a set of modes $\boldsymbol{\phi}_k(x, y)$ and temporal coefficients $a_k(t)$ along with energy levels E_k that weight the modes in terms of the amount of energy they contribute.

3. Flow dynamics

Our computational set-up is similar to that used in [23,24], and as we saw there we have several different flow regimes depending on Wi. In this paper we have studied cases for $4 \leq \text{Wi} \leq 12$ in increments of 0.25. For each case, we categorize the flow dynamics and show how the use of POD can aid in our understanding of the solutions as well as the categorization of the dynamics. For $\text{Wi} \leq 5$ the long time behavior of the flow is steady with two symmetries, left-right, and up-down, see Fig. 1 for example. For $5.25 \leq \text{Wi} \leq 6$ the flow loses one symmetry and the transient behavior includes oscillations that eventually are damped out, but the long time behavior of the flow is steady with one symmetry. For higher Wi the transient oscillations remain and the flow is unsteady. Both periodic and aperiodic behaviors are observed and we further characterize the types of behavior in terms of the dominant modes in the POD.

When the flow is time dependent the POD is very convenient for defining and understanding the different dynamics of the flows. Note here that the time range over which a POD is computed will effect the outcome of the decomposition. In particular if a flow has a transient from an unstable steady state to another state it is possible to include the transient to see the dynamics of the transition or exclude it to focus on the long-time dynamics. We will explore these different views of the solution for the cases we consider.

3.1. Steady solution (two symmetries): Wi ≤ 5

For $\text{Wi} \leq 5$ the flow evolves to a steady symmetric solution after a very short transient, $t \approx 20 - 50$. This transient arises in all the numerical experiments since the initial condition (a perturbation from isotropic

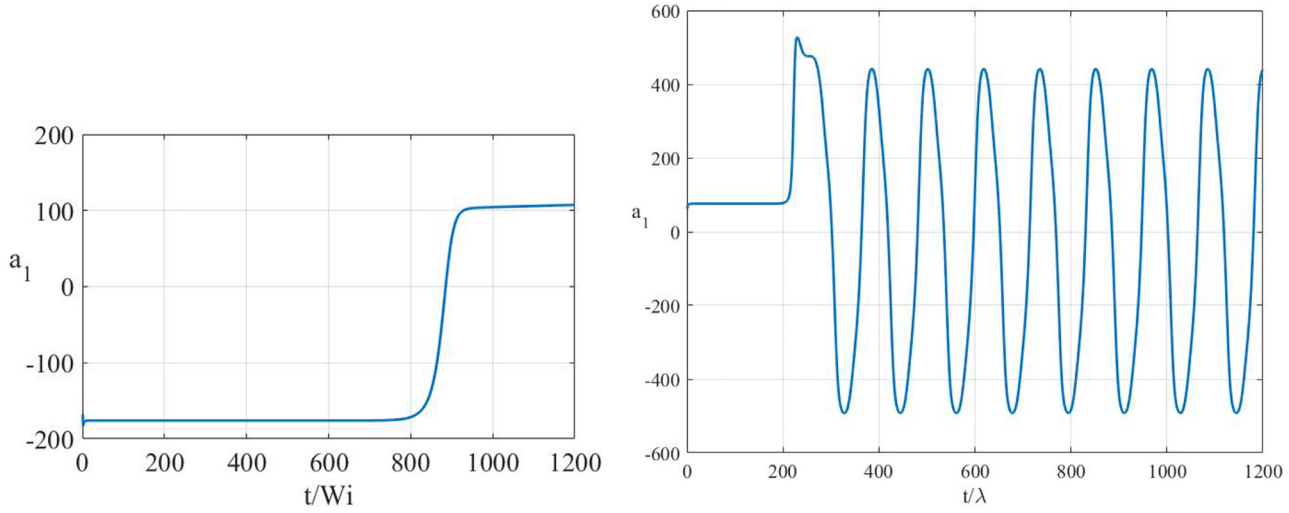

Fig. 2. First temporal mode, a_1, for the cases Wi = 5.25 (left) and Wi = 7 (right).

stress) is not a solution of the governing equations. This transient does not affect the long-time dynamics that we are categorizing. By choosing a fixed initial condition we are limiting the dynamics that we will explore to the stable solutions that arise from the chosen initial condition. A more complete exploration of this dynamical system is beyond the scope of this work. We will henceforth ignore this initial transient in our discussion of the solutions.

Fig. 1(a) shows contours of tr**S** for Wi = 5 at $t = 6000$. The trace of the conformation tensor tr**S** represents the amount of stretching of the immersed polymers, and is the strain energy density of the flow. The extensional point at the center creates symmetric stress islands that are elongated in the direction of stretching (horizontal) and concentrated in the direction of compression (vertical). There are two symmetries, about the lines $x = 0$ and $y = 0$. We include axes labels (x, y) as well as the domain $[0, 2\pi) \times [0, 2\pi)$ in this figure, but suppress these axes and axes labels for all future figures with contours of the stress and vorticity as they have the same domain.

Fig. 1(b) shows a snapshot of the vorticity at the same instant clearly demonstrating the 4-roll pattern characteristic for this problem configuration for small Wi number. Counter-vortices arise in the opposite direction along the direction of stretching to balance the stress. There are 8 stagnation points ($\mathbf{u} = (0, 0)$) in the domain, plus periodic copies. For small Wi these stagnation points are either pure extension (*type 1* in Fig. 1(c)) or pure rotation (*type 2* in Fig. 1(c)). For higher Wi the dynamics of the flow are connected with the movement of these stagnation points (as was seen in [24]). In what follows we highlight (in pink) a somewhat coarse threshold, $u^2 + v^2 \leq 10^{-4}$, to visualize regions near the stagnation points and track those regions through the complex flows that arise. When identifying the frequency of the stagnation points we trace the centroid of $u^2 + v^2$ and track the frequency of those points.

A POD decomposition is unnecessary when the flow is steady because the temporal mean is subtracted before computing the modes (see Eq. (6)) and deviations from the temporal mean are negligible.

3.2. *First transition: Movement of extensional stagnation points,* type 1

One of the main advantages of the POD is that the modes are extracted in the order of energy that they represent. For Wi ≥ 5.25 as the temporal evolutions evolve, the first mode of the POD of the entire time series always displays a jump when the temporal evolution first appears. This jump does not give information about what type of behavior will evolve, but indicates the onset of time-dependent solutions. As an example, Fig. 2 shows this first temporal mode for two different types of solutions. On the left, Wi = 5.25, the mode has a constant value until some time where a jump occurs and the mode continues with a different constant value. On the right, for Wi = 7, the mode clearly shows oscillatory behavior after the jump.

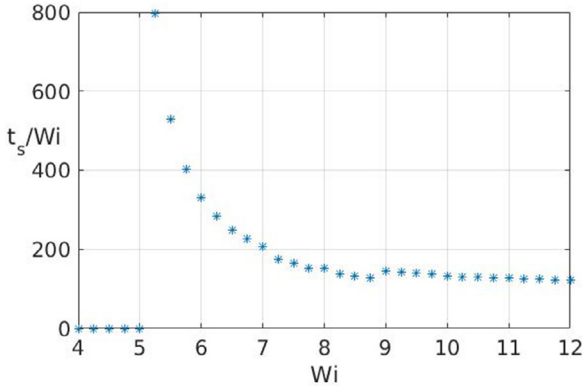

Fig. 3. Onset time (t_s) of time-dependence (normalized by Weissenber number Wi) as a function of Weissenberg number.

We can use the onset time of the time dependent behavior as a parameter to "see" the bifurcation to time-dependent states beyond Wi ≈ 5. We calculate the onset time of time-dependence, t_s, by selecting a change of 5% of the early time value of the dominant mode. Fig. 3 shows the starting time of the time-dependent solutions for the different Wi studied scaled with the relaxation time. In the bifurcation diagram, we see clearly how t_s/Wi diverges as Wi↘5.

Some of the cases we consider are more complicated to characterize than others, and they will be described further in the following sections using not only the first mode but all the relevant modes. A summary of the different solutions we find is presented in Table 1 which gives a flavor of the complexity of the problem. For each group of states, the required number of modes to capture 95% of the energy is calculated using different time intervals for the POD: considering the all the simulated time, and the late time of the flow once the long-time dynamics are established.

3.2.1. *Steady solution (one symmetry): 5.25 ≤ Wi ≤ 6.00*

We use data for Wi = 6 to represent the behavior in this range of Wi. Initially the flow is symmetric and qualitatively similar to the Wi = 5 case above, see Fig. 4(a), however now this symmetric solution is not stable. The loss of stability as Wi increases may be related to the fact that the maximum of the conformation tensor grows linearly with Wi [44,47]. At around $t \approx 1980$ ($t \approx 330$Wi) this unstable solution evolves to

Table 1
Categorization of flow states and number of modes needed to capture 95% of the energy over different time periods.

Wi range	# Flow transitions	Long-time dynamics	# a modes all times	# a modes late times
Wi = 4.00 – 5.00	0	Steady 2 symmetries	0	0
Wi = 5.25 – 6.00	1	Steady 1 symmetry	1–2	0
Wi = 6.25 – 7.75	1	Periodic (oscillatory)	3–6	4–5
Wi = 8.00 – 8.75	1	Periodic (loop)	6–8	6
Wi = 9.00 – 10.25	2	Aperiodic	9–14	11–13
Wi = 10.50 – 12.00	2	Periodic (dominant vortex)	6	4

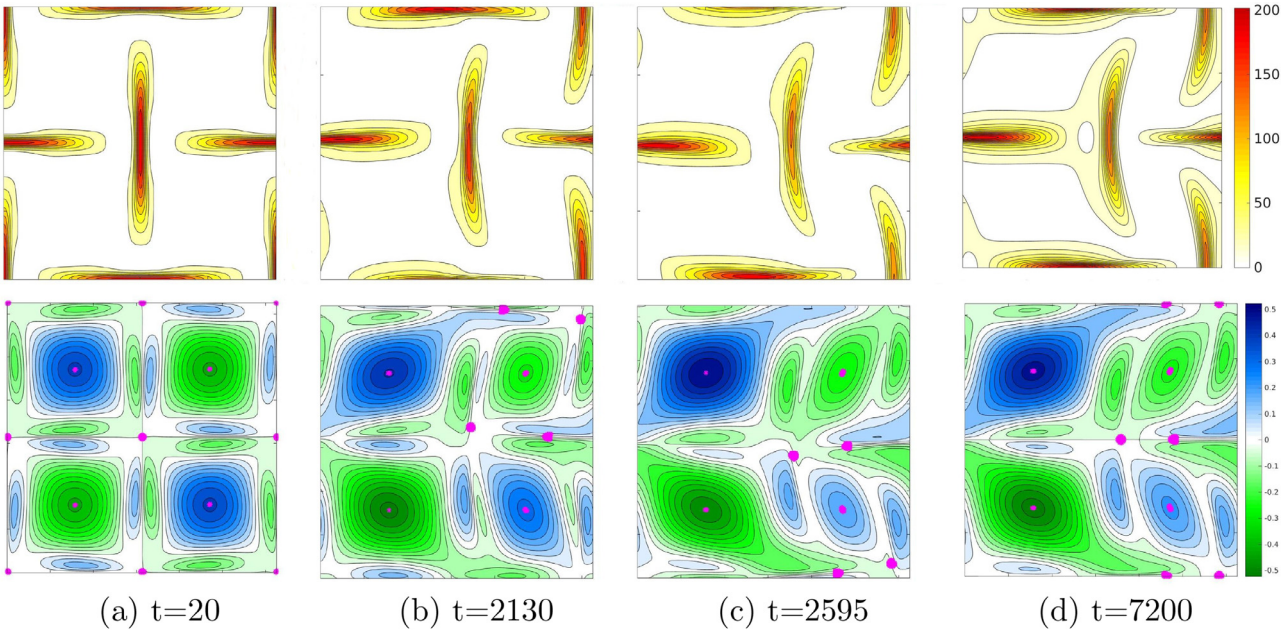

Fig. 4. Time evolution of Wi = 6. tr**S** in the first row and vorticity superimposed with the stagnation points in the second row.

an oscillatory state. As the symmetric solution loses stability the extensional stagnation points (*type 1*) begin to oscillate in the $\pm y$ direction.

The stagnation points are shown in pink in Fig. 4 in the second row superimposed on contours of the vorticity. Fig. 4(b) is a snapshot at the time of the first peak of the oscillation, and it is possible to see the oscillation by examining the location of the stagnation points in the vorticity. We also see that the center island in tr**S** is bent to the right and oscillates in the vertical direction. The oscillations decrease in time and eventually the solution converges to a new steady state which has only one spatial symmetry (in the vertical direction). Details can also be seen in the supplementary information online where movies for tr**S** and vorticity of all the representative cases are included. We ran this simulation until $t = 2000\text{Wi}$ to ensure that it has converged to a steady state. We see the same symmetry in the vorticity with the stagnation points highlighted in Fig. 4. During the transient the 4-rolls lose symmetry in the y–direction. The loss of up-down symmetry is dependent on the initial conditions, thus rotations of this case are possible for other initial conditions. This type of symmetry breaking instability was first observed experimentally near the extensional stagnation point in a cross-slot geometry [9].

We use a POD to characterize the time-dependent motion for Wi = 6 over three different time ranges with $\Delta t = 5$ in each case: $t = 0 - 1200\text{Wi}$, $t = 1000\text{Wi} - 1200\text{Wi}$, and $t = 1800\text{Wi} - 2000\text{Wi}$. First, we describe the POD over the entire time series. Two modes are sufficient to capture 95% of the energy in this case, see Fig. 5(a). The first mode, a_1, is steady in the initial symmetric period with a jump at the onset of the time-dependence, meanwhile the time-dependent damped oscillations are captured by the second mode, a_2. We also find that the frequency associated with the second mode is the same frequency as the vertical displacement of the extensional stagnation points of *type 1*. This can be seen in Fig. 5(b) where we plot mode a_2 (right axis) as well as the vertical position of the center stagnation point, y_c (left axis) over the same time period.

We get a different view of the solution by doing a POD for later times. Now we perform the decomposition for $t = 1000\text{Wi} - 1200\text{Wi}$. Again two modes are required to capture 95% of the energy, but in this case there is no transient. The percent of the energy in each of the modes is shown in Fig. 6(a), and the temporal structure of the modes is shown in Fig. 6(b).

We turn now to the spatial information in the POD. Recall that the spatial modes are given in terms of b_{ij}, but the conformation tensor involves the square, $\mathbf{S} = \mathbf{b}^2$. For example we have

$$\text{tr}\mathbf{S} = b_{ij}^2 = b_{11}^2 + 2b_{12}^2 + b_{22}^2. \tag{10}$$

Thus (from Eq. (6)) one needs information from all of the components of **b** as well as the mean to reconstruct tr**S**. We display the mean and the two modes for each component of **b** in Fig. 7. We remark that the geometric modes have roughly the same spatial complexity as the stress at an instant in time. We can quantify this by examining how many Fourier modes are needed to represent the solution to some level of accuracy and find that a comparable number of Fourier modes are needed for the geometric modes and for the full solution at some instant in time.

Since the temporal mode is oscillatory, the oscillations we saw in tr**S** in Fig. 4 come from the periodic addition and subtraction of the b_{ij} modes to the mean. The first mode clearly shows vertical oscillations, and the second mode represents (much smaller in energy) left/right oscillations.

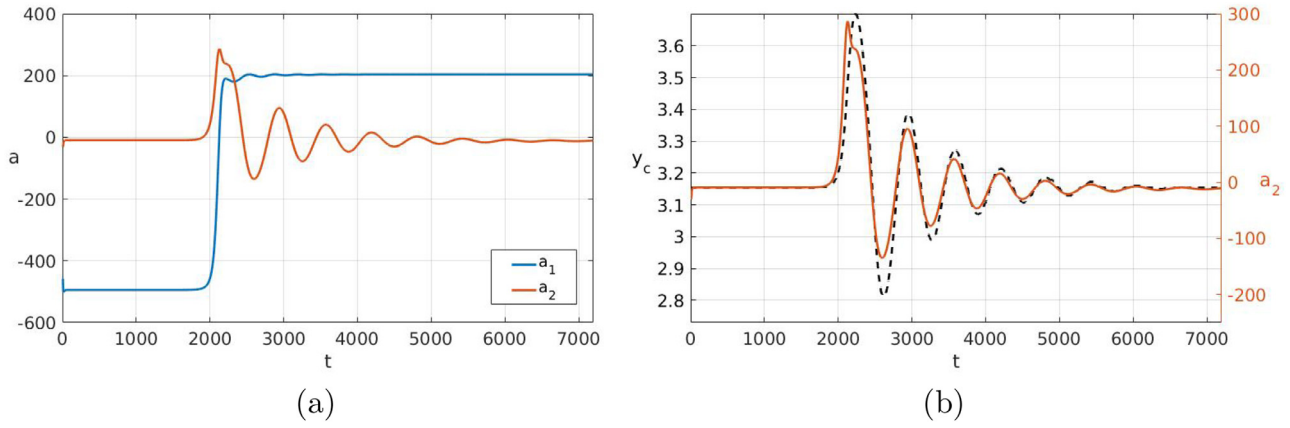

Fig. 5. (a) Temporal modes for Wi = 6 obtained with POD in the range $t = 0 - 1200$Wi, with $\Delta t = 5$, (b) position of the central stagnation point (left axis) and a_2 mode (right axis) of Wi = 6 obtained with POD in the range $t = 0 - 1200$Wi, with $\Delta t = 5$.

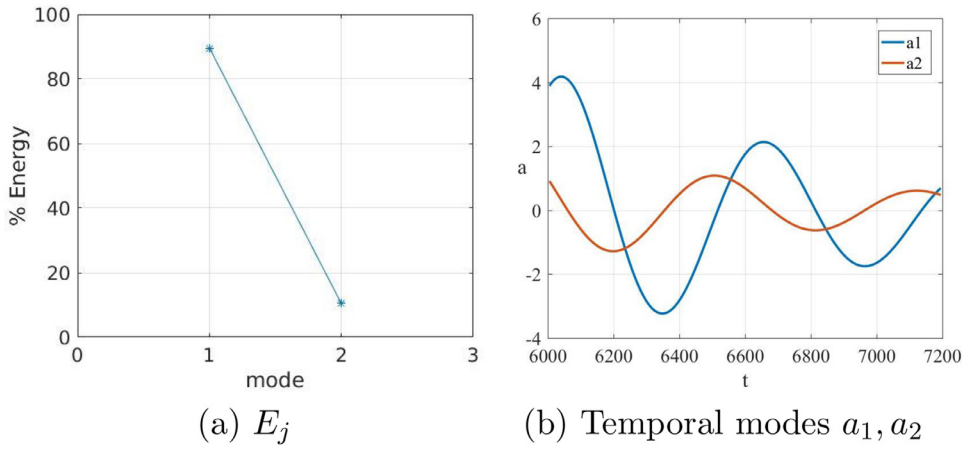

Fig. 6. Features obtained from the POD for Wi = 6 for times between 1000Wi – 1200Wi, with $\Delta t = 5$.

The long-time behavior in this case is steady and hence a POD at sufficiently long times will not generate any modes since the difference between the flow and the mean are negligible. In this case we used $t = 1800$Wi – 2000Wi.

3.2.2. *Periodic solution (oscillatory): 6.25 ≤ Wi ≤ 7.75*

We look at Wi = 7 as a representative solution in this regime. For Wi = 6 we saw an initial symmetric long time transient which became unstable with damped oscillations that eventually died out leading to a long time steady case with one symmetry. For Wi = 7 oscillations do not get damped, and the long-time behavior of the solution is periodic. Furthermore, the oscillations are observably both in the vertical direction and the horizontal direction.

Fig. 8 shows snapshots of tr**S** and vorticity over one period once the flow has converged to a periodic state. The flow for Wi = 7 has lost both the vertical and horizontal symmetry and now over a period we see oscillations between near up-down symmetry with two dominant vortices in the left cells and near left-right symmetry with two dominant vortices in the top cells. This flow is stably periodic although it has similarities with the single symmetry flow for Wi = 6. In particular the flow state in Fig. 8(a) is similar to that from Fig. 4(d).

We show results of a POD using temporal data over 5 periods of the long-time behavior in Fig. 9. Here 5 modes capture 95% of the energy with the first mode having about 67%$\mathbf{E}_{ve}$. The next 4 modes come in pairs with modes 2&3 having about 10%$\mathbf{E}_{ve}$ each and 4&5 having about 5%$\mathbf{E}_{ve}$ each. We plot the time-series of the first 3 modes in Fig. 9(b) and see that the modes all have the same frequency.

Fig. 10 shows the temporal mean and three geometric modes for b_{ij}.

The first mode shows a left-right oscillation in b_{11} and a up-down oscillation in b_{22}. The b_{12} mode contributes to rotations. The pairs of modes 2&3 will represent traveling structures and there are symmetries in these modes as well, e.g. mode 2 of b_{11} reflected by $x = y$ axis and displaced by π gives mode 3 of b_{22} and similarly between mode 3 of b_{11} and mode 2 of b_{22}.

3.2.3. *Periodic solution (loop): 8.00 ≤ Wi ≤ 8.75*

Like Wi = 7, the solutions for 8.00 ≤ Wi ≤ 8.75 are also periodic, but now the flow has transitioned again. We describe the flow for Wi = 8 as a representative from this group. In this case there is an initial transient where the solution behaves like Wi = 7, but eventually a new periodic state evolves where the dominant vortex "loops" around all 4-rolls, rotating clock-wise (in this case). Fig. 11 shows the time evolution of the vorticity in a period where the loop can be seen. Note that the period is very long, $T \approx 1210$.

A POD is performed over 5 periods, and the energy in the modes is shown in Fig. 12(a). Now the first two modes contribute equally (each about 35%) to the energy. Note that pairs of modes typically represent traveling structures, and in this case we see the vortices and other flow features rotating through the quadrants. The time-series, Fig. 12(b) shows that these two first modes are periodic with the same period, with a phase-lag. The higher modes also have the same frequency.

The temporal mean of all the **b** components is shown in Fig. 13 first column. Again we find a symmetry where one can obtain the mean of b_{22} from b_{11} with a shift and reflection over $y = x$. Note that in this case that the relative difference between b_{11} and b_{22} (modulo the symmetry) is less than 1%. Modes 1 and 2 also have such symmetries.

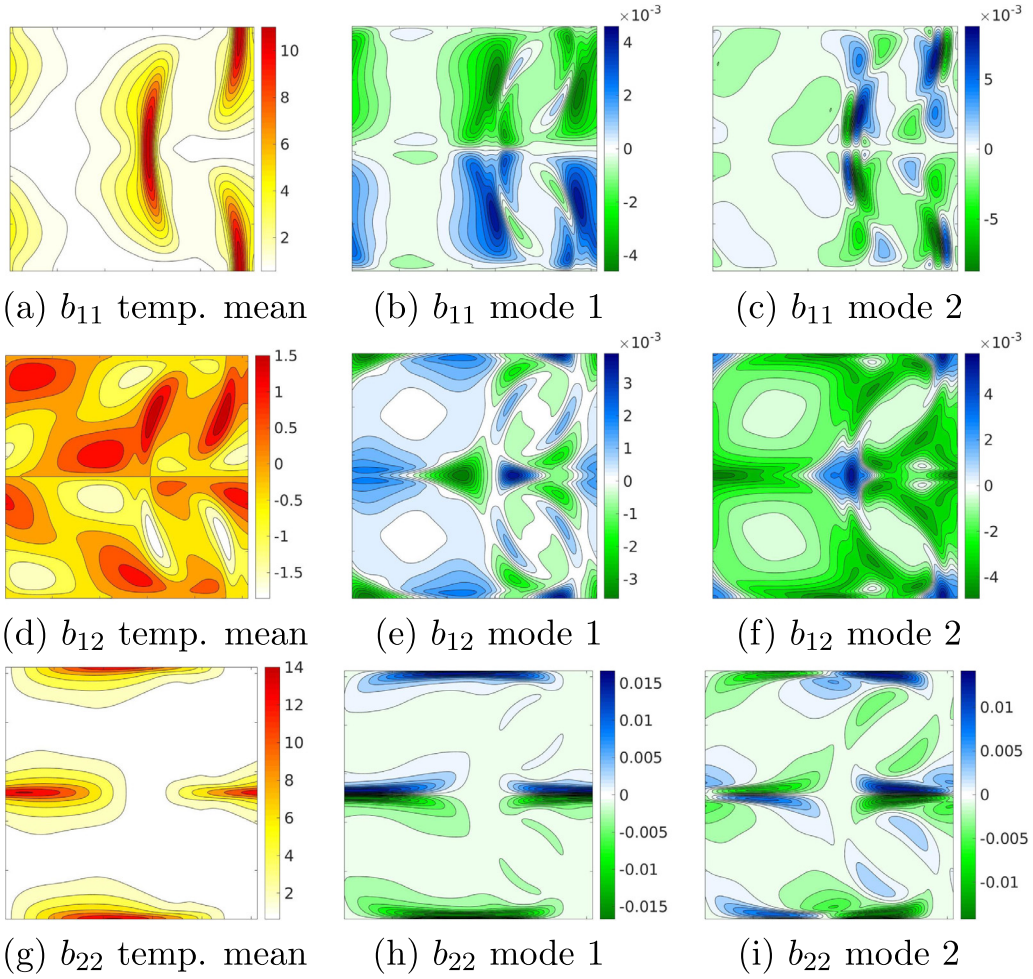

Fig. 7. Features obtained from the POD for Wi = 6 for times between 1000Wi – 1200Wi, with $\Delta t = 5$.

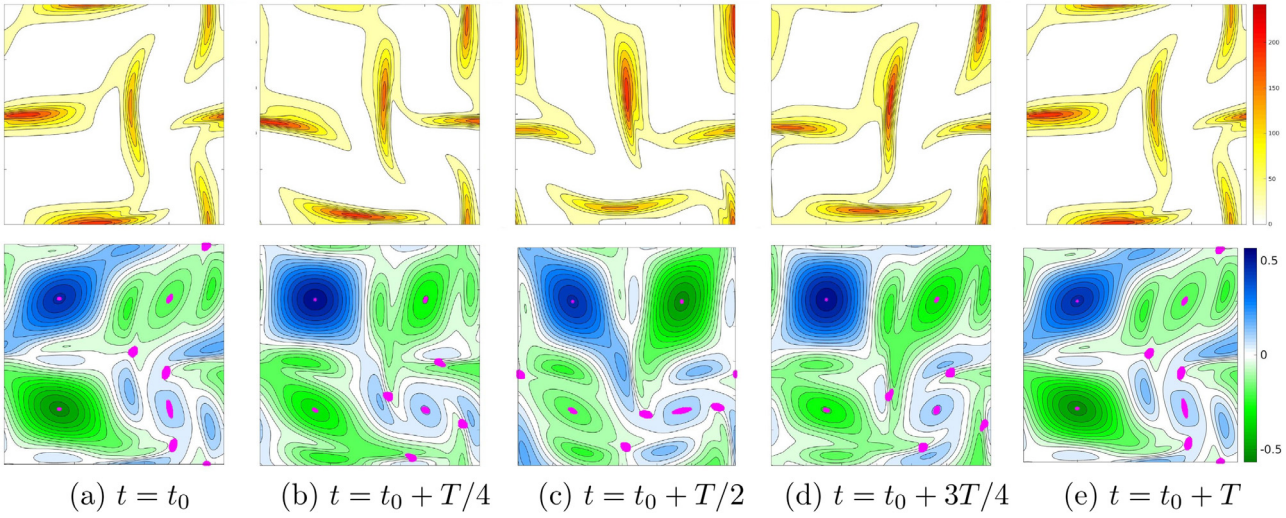

Fig. 8. Time evolution of Wi = 7. tr**S** in the first row and vorticity superimposed with the stagnation points in the second row.

3.3. Second transition: Movement of rotational stagnation points, type 2

For cases with Wi ≥ 9 the flow presents a new kind of solution. The temporal evolution can be described as follows. There is a transient similar to the Wi = 5 solution, after which there is a change in behavior associated with the displacement of the extensional stagnation points (*type 1*) (starting in the center of the domain). Later there is a second transition associated with the movement of the rotational stagnation points (*type 2*) (moving from the centers of the quadrants). The frequencies of the motion of the stagnation points now leads to two qualitatively different types of flows, described below.

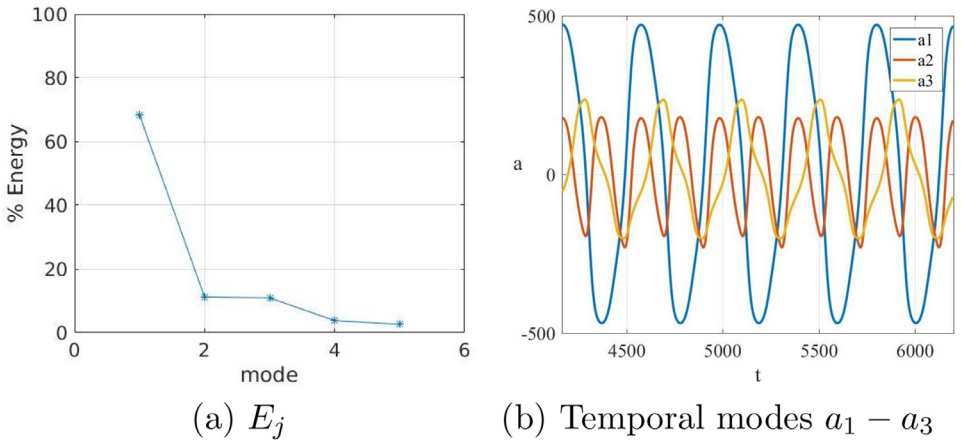

(a) E_j (b) Temporal modes $a_1 - a_3$

Fig. 9. Features obtained from the POD decomposition of Wi = 7 using five periods, $T \approx 815$, with $\Delta t = 5$.

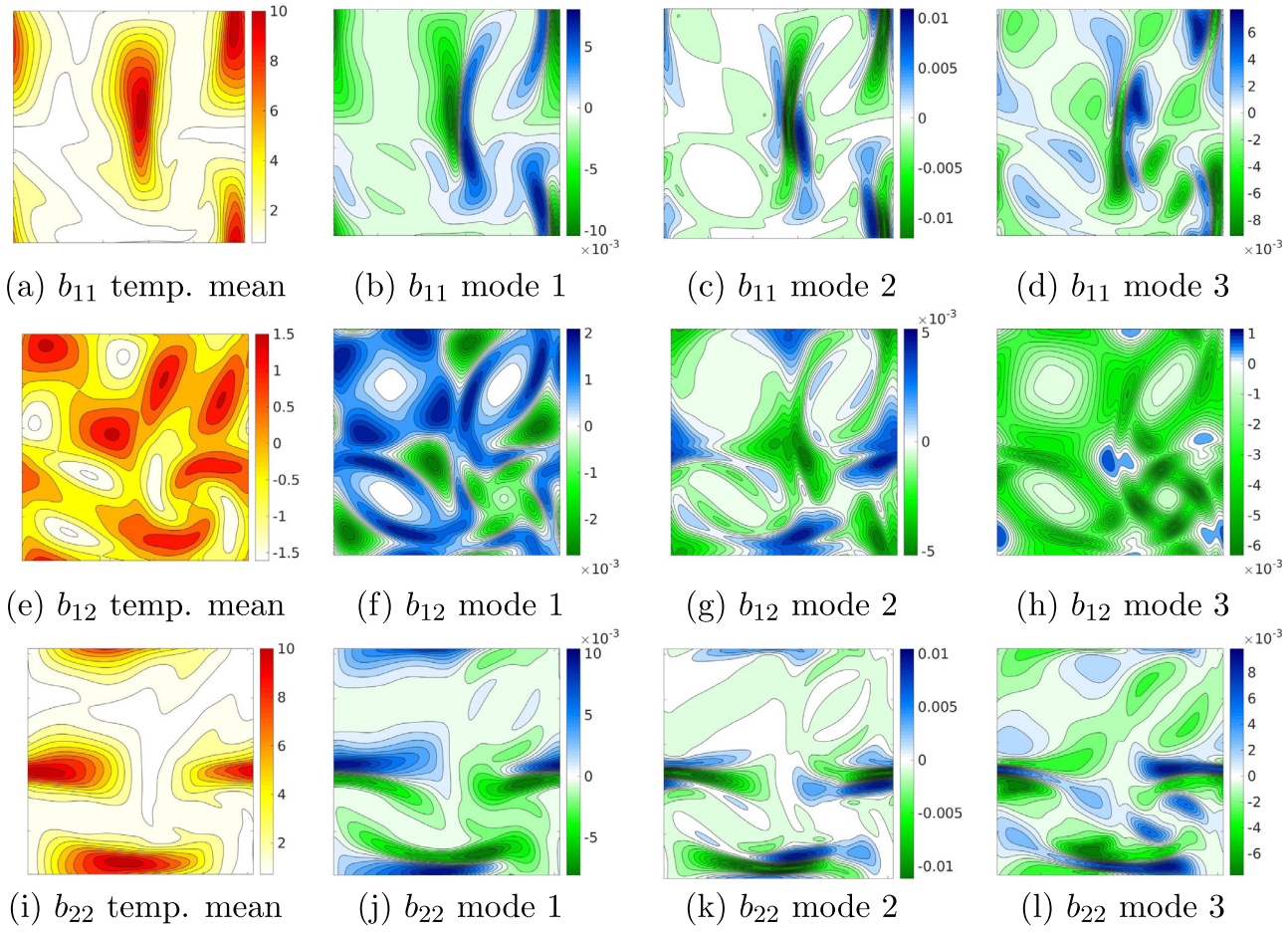

(a) b_{11} temp. mean (b) b_{11} mode 1 (c) b_{11} mode 2 (d) b_{11} mode 3

(e) b_{12} temp. mean (f) b_{12} mode 1 (g) b_{12} mode 2 (h) b_{12} mode 3

(i) b_{22} temp. mean (j) b_{22} mode 1 (k) b_{22} mode 2 (l) b_{22} mode 3

Fig. 10. Features obtained from the POD decomposition of Wi = 7 using five periods, $T \approx 815$, with $\Delta t = 5$.

3.3.1. Aperiodic solution: $9 \leq Wi \leq 10.25$

We use Wi = 10 to represent the flows for this range of Wi. After the transient, a big dominant vortex is created in the bottom left corner (again other possible orientations are possible from different initial conditions) at $t \approx 1300$, and later, around $t \approx 3600$ higher frequency oscillations arise in the flow. The flow is not periodic and the POD demonstrates this clearly with many more modes needed to capture the energy and aperiodicities in the temporal coefficients. For example, when computing a POD over the time $t = 0 - 1200$Wi we see that 13 modes are needed to capture 95% of the energy, see Fig. 14(a). However, much of the relevant information can be obtained by using the first four modes which capture 83%$\mathbf{E}_{ve}$. In Fig. 14(b) we plot the first 3 temporal modes a_1, a_2, and a_3 for a POD computed over the time $t = 0 - 1200$Wi (mode a_4 is similar to a_3). As we saw for all Wi ≥ 6 the first mode is the shift mode representing the initial transient from symmetric to asymmetric. Mode a_2 shows the onset of the oscillations of *type 1* when the symmetry break occurs. The higher frequency oscillations occur around $t \approx 3600$ when the stagnation points of *type 2* being to move, and these oscillations are captured by a_3.

Focusing now on the long-time behavior, we can define a near-period of the flow for Wi = 10 by looking at the POD of the flow after the second transition, for example for $t = 1000$Wi $- 1200$Wi, and using an approxi-

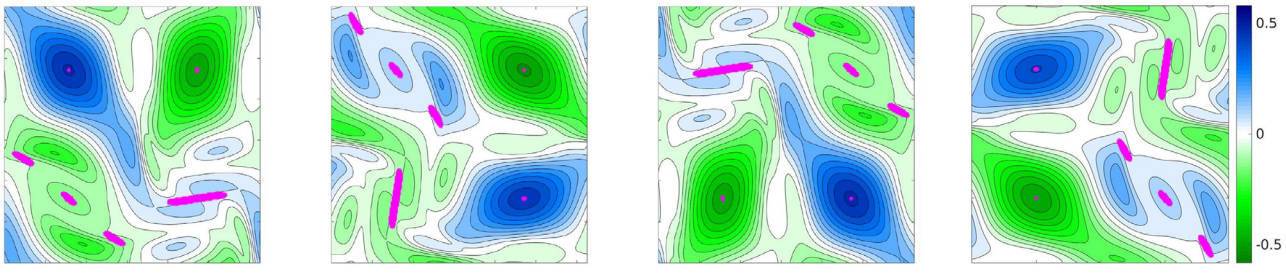

Fig. 11. Time evolution of vorticity superimposed with the stagnation points for Wi = 8.

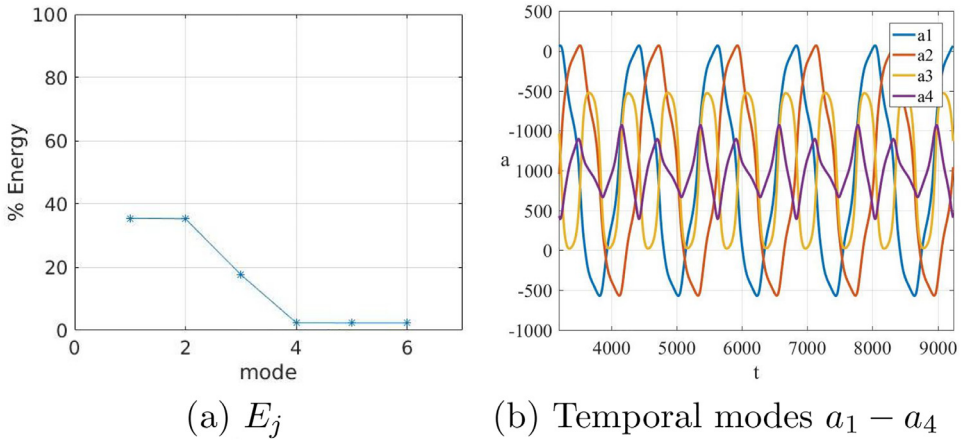

Fig. 12. Features obtained from the POD decomposition of Wi = 8 using five periods, $T \approx 1210$, with $\Delta t = 5$.

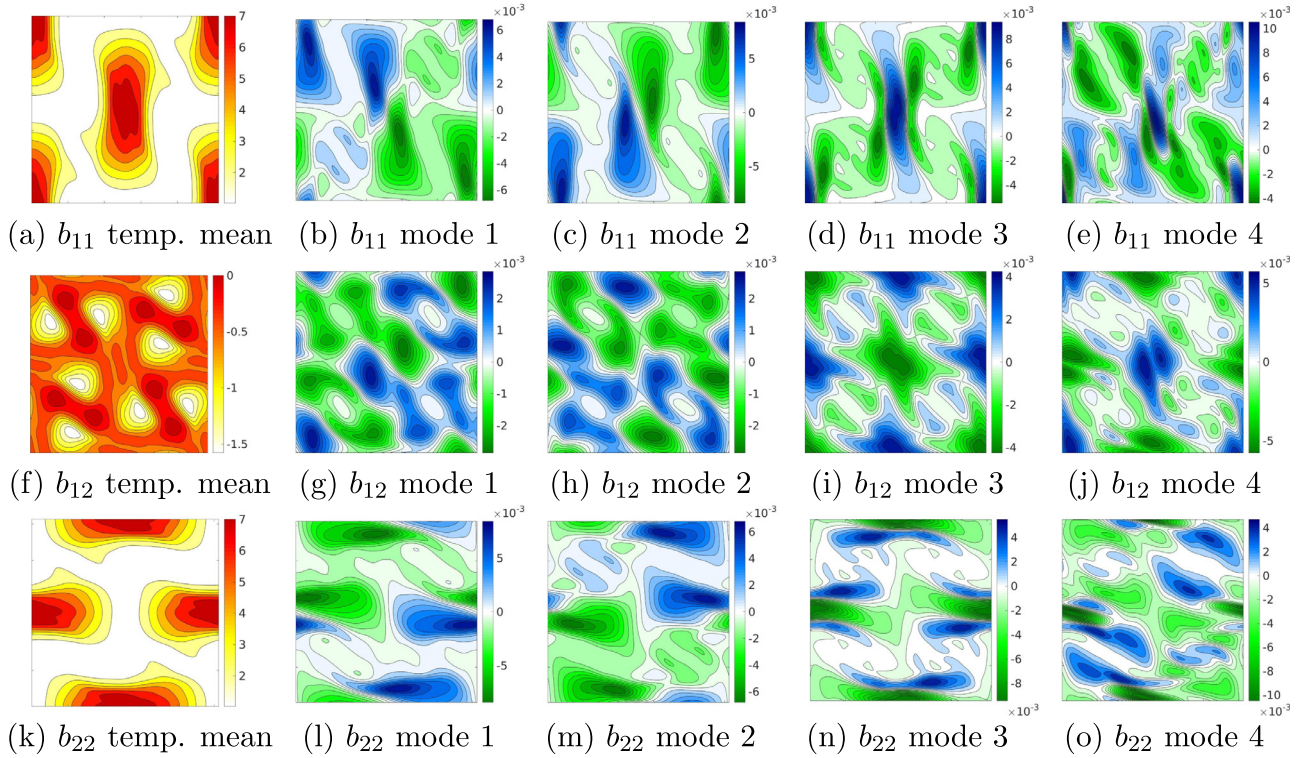

Fig. 13. Features obtained from the POD decomposition of Wi = 8 using five periods, $T \approx 1210$, with $\Delta t = 5$.

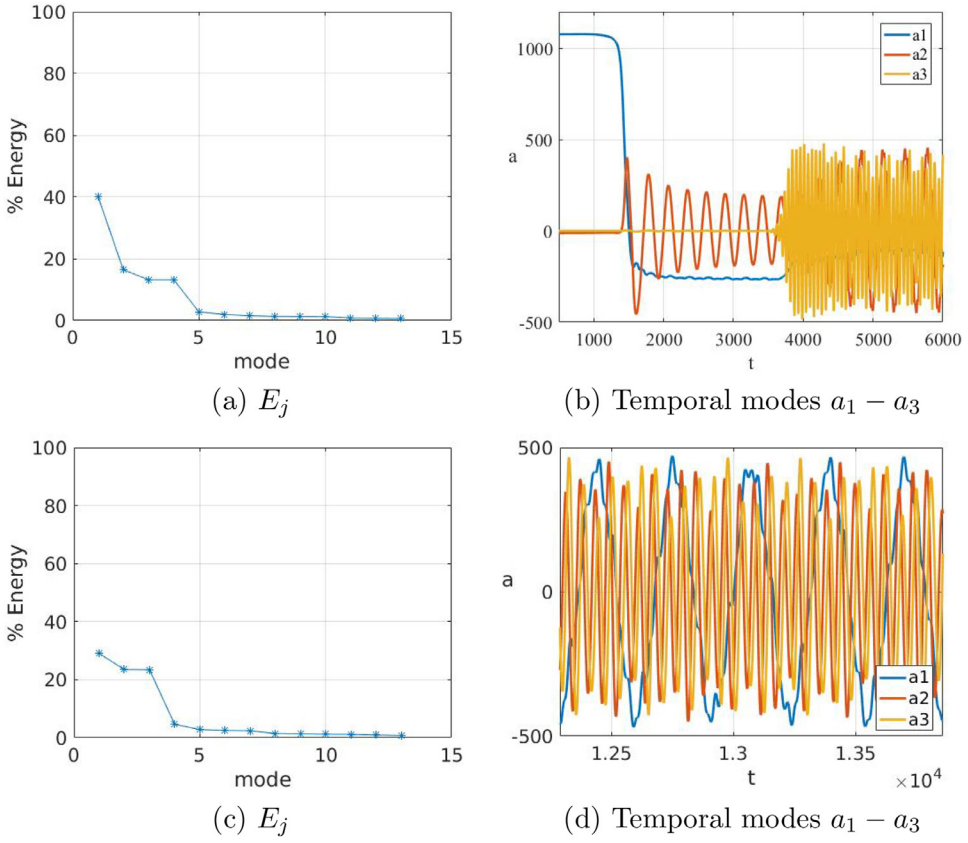

Fig. 14. Features obtained from the POD decomposition for Wi = 10. (a)-(b) POD over $t = 0 - 1200$Wi, with $\Delta t = 5$, (c)-(d) POD over $5T_{\text{mode}\,1}$, with $T_{\text{mode}\,1} \approx 314$, with $\Delta t = 0.1$.

mation of the period of the highest energy mode at these late times in the flow, obtaining $T_{\text{mode}\,1} \approx 314$. We then use this $T_{\text{mode}\,1}$ to compute the POD over $5T_{\text{mode}\,1}$, and show the energy in the modes in Fig. 14(c).

While 13 modes are needed to capture 95% of the energy, the flow is now dominated by the first 3 modes, this time capturing 76%$\mathbf{E}_{\text{ve}}$. The temporal evolution of these modes over late times, is shown in Fig. 14(d). For this long-time behavior the shift mode does not appear. Now we find that the frequencies of the first two modes are the same as the frequencies of the oscillations of the stagnation points of *type 1* and *type 2*. We find $T_{\text{mode}\,1} \approx 314$ and $T_{\text{mode}\,2} \approx 57$, these two frequencies are not multiples of each other, and this creates the aperiodicity in the flow. Note that the POD decomposition was computed with a very small time interval $\Delta t = 0.1$ to avoid any imprecision caused by calculating the POD decomposition with $\Delta t = 5$, with little change in the result. We conclude that it is not possible to represent this kind of solution with periodic modes.

Fig. 15 shows snapshots of contours of tr**S** over time. The initial transient shows oscillations in the stress concentration with a dominant vortex in the bottom left corner. The second temporal transition has led to a qualitatively different flow state where the stress concentration appears to rotate within the dominant vortex with a period that is not a multiple of the oscillations. The snapshots are plotted at fractions of $T_{\text{mode}\,1}$, and we can see that the motion is not periodic.

The temporal mean and first three geometric modes of **b** are shown in Fig. 16. These modes display the same features associated with oscillations and rotations as have been seen previously. It is the temporal structure of the modes, i.e. the frequencies are not multiples of one another, that causes the flow complexity.

3.3.2. *Periodic solution (dominant vortex): 10.5 ≤ Wi ≤ 12.*

In this range we find that the solutions are once again periodic, here we use Wi = 12 to represent the solutions in this range. The temporal evolution of this solution has an initial transient with two symmetries followed by oscillations in the stagnation points of *type 1*. Unlike Wi = 10, these oscillations decay nearly to zero leading to an unstable asymmetric steady state. This is followed later by another transition when the stagnation points of *type 2* oscillate. In this case, the oscillations in the stagnation points of *type 1* and *type 2* have the same frequency, and the solution is periodic. We show snapshots of tr**S** over a period in Fig. 17.

In this case we present results of the POD over 5 periods of the long-time behavior. For this periodic flow, four modes capture 95% of the energy as it is shown in Fig. 18(a). The modes come in pairs with a_1 and a_2 having the same energy as do a_3 and a_4. The temporal behavior is shown in Fig. 18(b). We see that modes a_3, a_4 have double the frequency of modes a_1, a_2.

In Fig. 19 we plot the geometric modes and we can see again how the full solution can be constructed out of minimal information. We note that $\Delta t = 1$ was used in this case to get the appropriate temporal resolution since the frequency of the motion is high. Due to the simplicity of this flow, only 6 modes are needed to represent the full solution including both transients.

4. Spatio-temporal error in approximation with POD

The POD is an approximation of the solution in terms of the energy, but here we consider a measure of the error in the approximation of the solution in both space and time. The viscoelastic POD at zero-Reynolds number gives the elastic modes for **b**, and the modes for **S** involve the squares of the modes of **b**. For each b_{ij}, $1 \le i \le j \le 2$, we define an approximation for b_{ij} with r modes:

$$\tilde{b}^r_{ij} = \bar{b}_{ij}(x, y) + \sum_{k=1}^{r} a_k(t) b^{\phi_k}_{ij}(x, y), \tag{11}$$

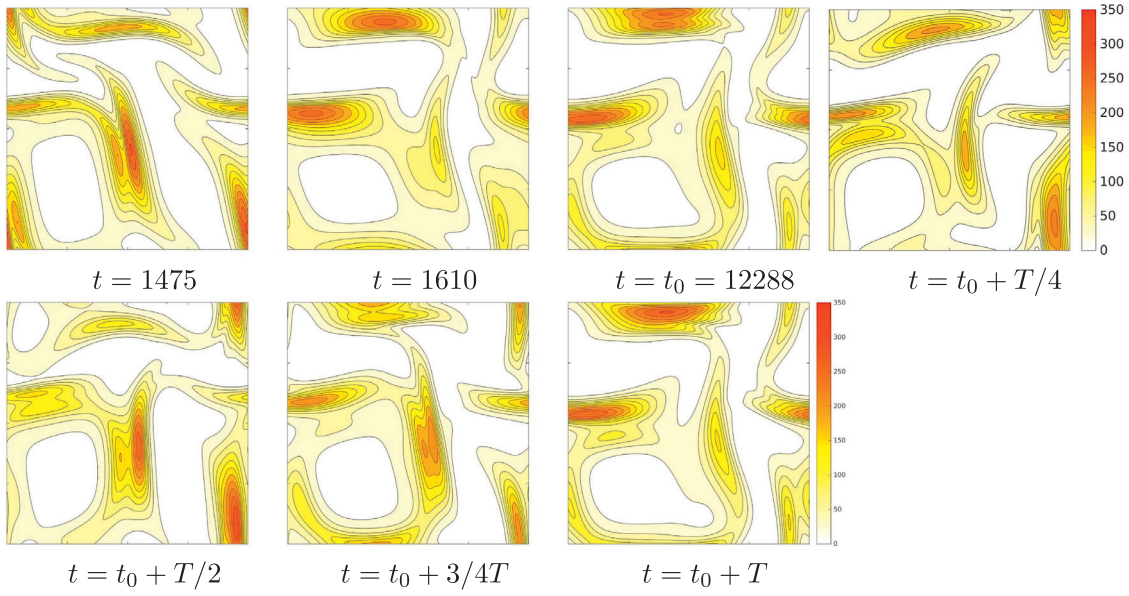

Fig. 15. Time evolution of tr**S** for Wi = 10, non-periodic solution.

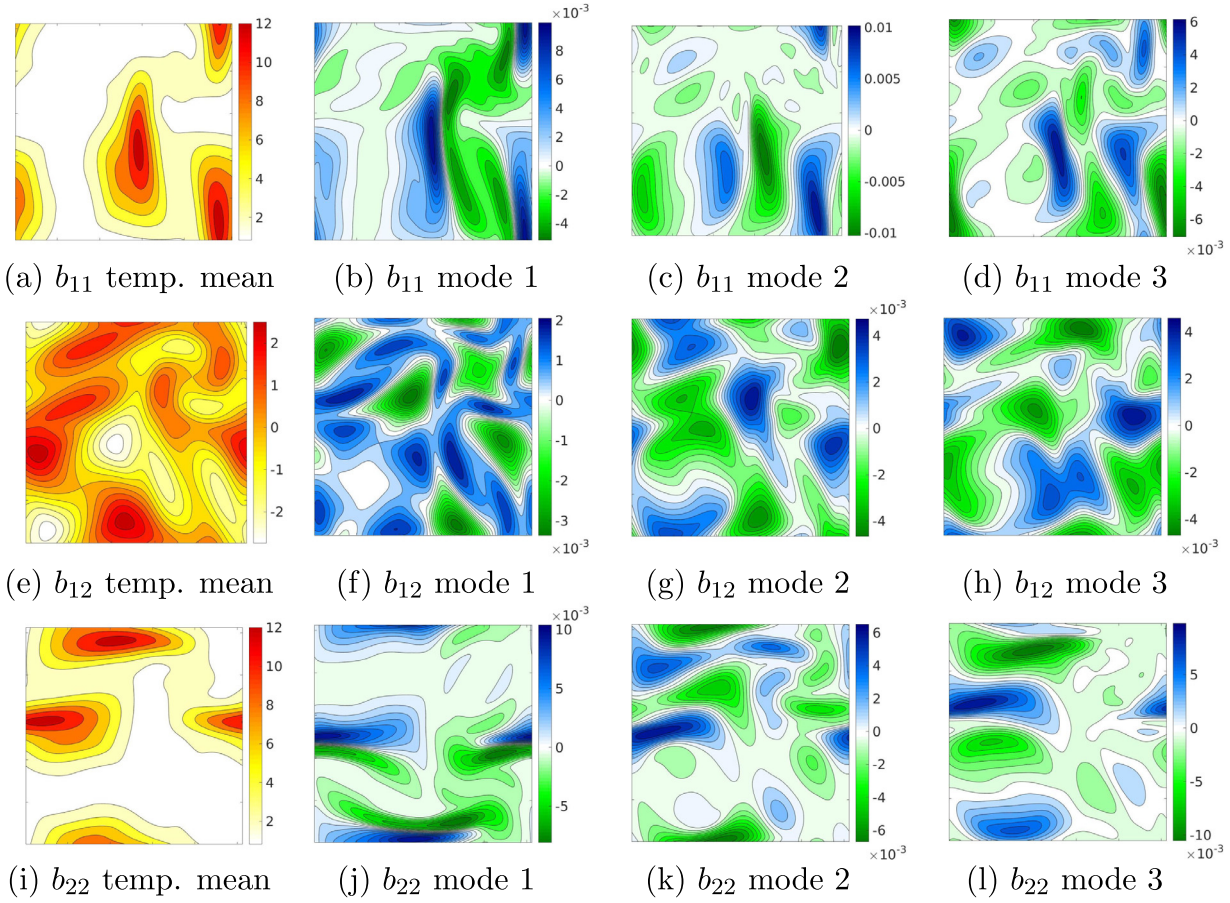

Fig. 16. Features obtained from the POD decomposition of Wi = 10 using five $T_{\text{mode 1}} \approx 314$, with $\Delta t = 0.10$.

where $b_{ij}^{\phi_k}$ is the geometric mode for b_{ij} coming from ϕ_k, and $\bar{b}_{ij}(x, y)$ is the temporal mean of b_{ij}. With this we define

$$\tilde{S}_{ij}^r = \tilde{b}_{ik}^r \tilde{b}_{kj}^r. \tag{12}$$

to be the approximation of S_{ij}, with r modes.

We compare the approximate solution $\text{tr}\widetilde{\mathbf{S}}^r$ using r modes (i.e. the number of modes needed to capture 95%$\mathbf{E}_{\text{ve}}$) with the full solution tr**S**, and define the relative error in this approximation as

$$\text{Rel. error} = \text{mean}_{\text{time}} \frac{\|\text{tr}\mathbf{S} - \text{tr}\widetilde{\mathbf{S}}^r\|}{\|\text{tr}\mathbf{S}\|}, \tag{13}$$

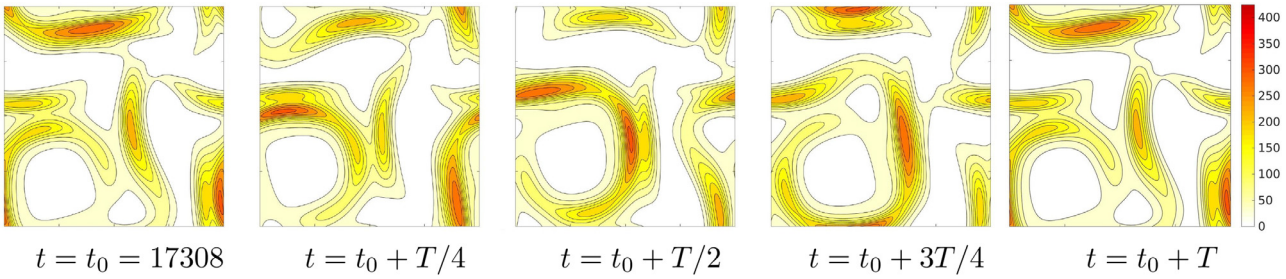

Fig. 17. Time evolution of tr**S** for Wi = 12, periodic solution.

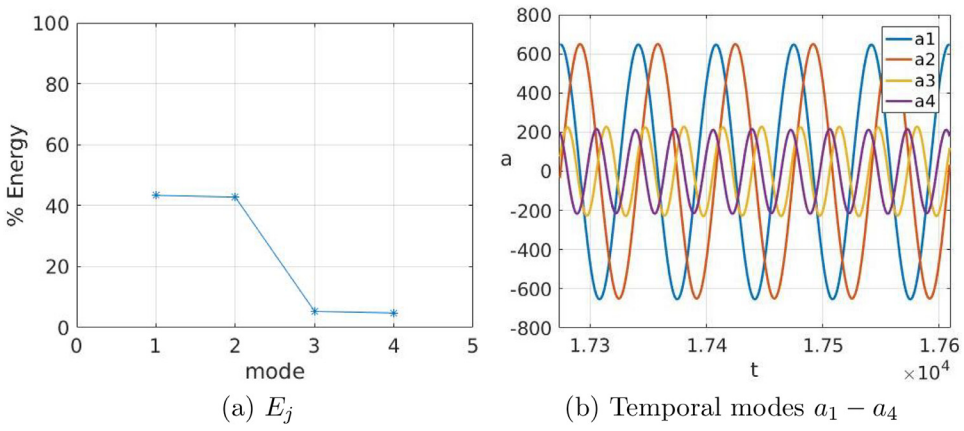

Fig. 18. Features obtained from the POD decomposition of Wi = 12 using 5 periods of the last temporal behavior, $T \approx 66$ with $\Delta t = 1$.

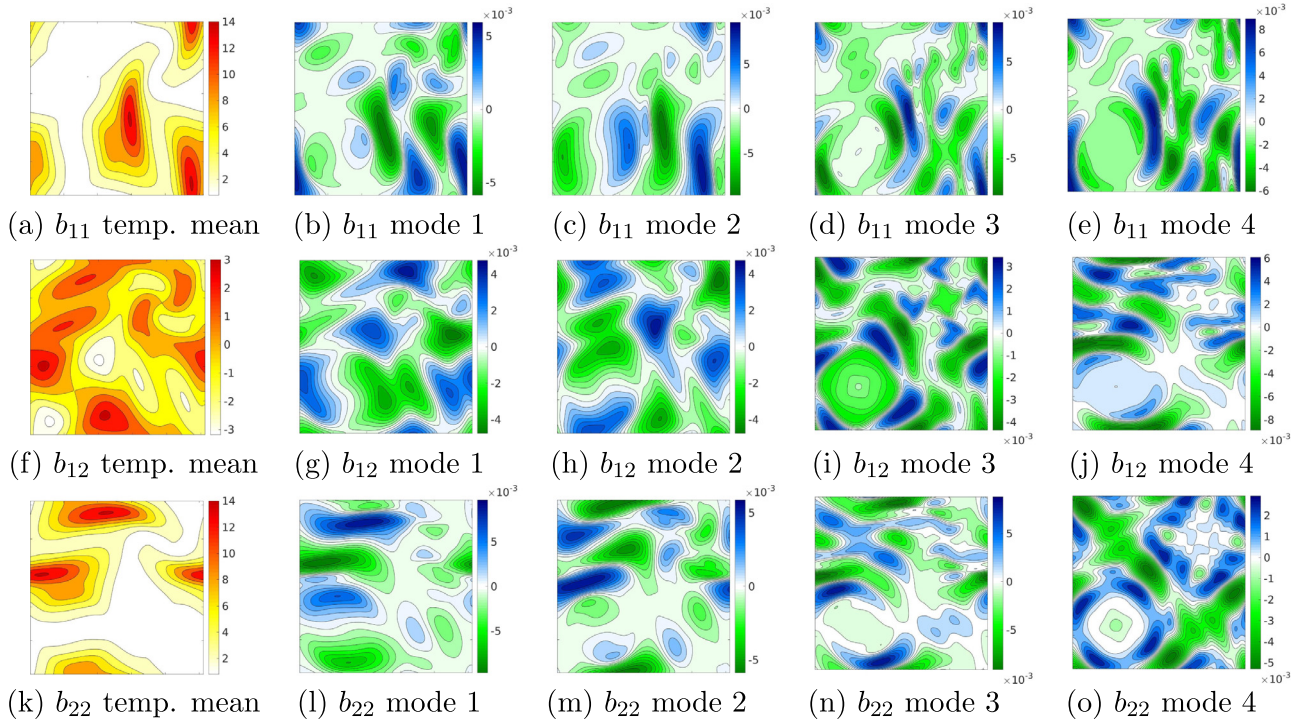

Fig. 19. Features obtained from the POD decomposition of Wi = 12 using five periods, $T \approx 66$ with $\Delta t = 1$.

where $\|\cdot\|$ is the L^2 norm. In each case we reconstruct using a POD over $t = 0 - 1200$Wi with $\Delta t = 5$. The errors are listed in Table 2. In all cases the error is around 10%, largest for Wi = 8 which has the large-scale traveling vortices. It is also quite small for the case Wi = 6 which only involves a transient between two steady cases. This shows that the energy decomposition gives a reasonably good approximation for the flow over the time series in terms of differences at a fixed point in space and time.

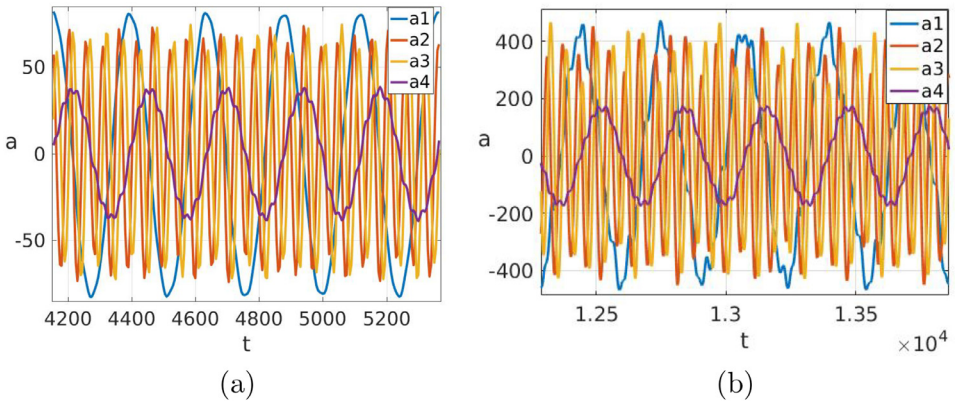

Fig. 20. Features obtained from the POD decomposition using $5T_{\text{mode 1}}$ of the last temporal behavior. (a) FENE-P for Wi = 12, with $T_{\text{mode 1}} \approx 250$. (b) Oldroyd-B for Wi = 10, with $T_{\text{mode 1}} \approx 314$.

Table 2
Relative error for $\text{tr}\tilde{\mathbf{S}}$, and the number of modes needed to capture 95%$\mathbf{E}_{\text{ve}}$ over the whole time series $0 - 1200$Wi using $\Delta t = 5$.

Wi	Rel. error	# of modes for 95%$\mathbf{E}_{\text{ve}}$
6	3.4%	2
7	9.07%	6
8	13.15%	8
9	8.78%	9
10	9.43%	13
11	9.44%	6
12	9.81%	6

5. FENE-P model

The results in the previous sections are calculated for a fixed grid with added polymer stress diffusion to regularize the solutions. We have checked that upon refinement if we *fix* the stress diffusion we obtain the same solution dynamics, but the dynamics do change quantitatively (and may change qualitatively) when the diffusion is grid-dependent. However, when the stress diffusion is fixed independently from the grid, the set of equations does not converge to the Stokes–Oldroyd-B system as $dx \to 0$. Fixed diffusion as a numerical regularization will set a length-scale for max $\text{tr}\mathbf{S}$, as well as for the width of the stress islands that concentrate in the direction of compression (at least in the symmetric transient of the solution [44,47]). The influence of artificially large stress diffusion on the dynamics of elastic turbulence is considered in a recent paper [48]. There are many other types of numerical regularizations that have been used to make solutions of the Stokes-Oldroyd-B equations more robust (see [8] for a nice review of numerical method for viscoelastic fluids). In addition there are many other models that one can use to enforce finite extension, such as FENE-P or other FENE models [41,49,50], and many different models with some sort of nonlinear relaxation term that will effect how the stress grows at extensional points such as the Giesekus [51] or PTT models [52]. In the case of a steady extensional flow such as the 4-roll mill geometry considered here, some numerical regularization is still necessary in the FENE-P, Giesekus, and PTT models [19,53] to obtain long-time solutions. However, in the 4-roll mill geometry, beyond the transition to unsteady solutions, no artificial diffusion was needed to simulate the flow dynamics with FENE-P using the square-root method [46].

To demonstrate that with other models we can recover qualitatively similar results to those described above, we run simulations with the FENE-P model and perform a POD of the obtained data. The FENE-P model is given by

$$\Delta\mathbf{u} - \nabla p + \beta\nabla\cdot\mathbf{S} = \mathbf{f}, \tag{14}$$

$$\nabla\cdot\mathbf{u} = 0 \tag{15}$$

$$\partial_t\mathbf{C} + \mathbf{u}\cdot\nabla\mathbf{C} - \left(\nabla\mathbf{u}\mathbf{C} + \mathbf{C}\nabla\mathbf{u}^T\right) + \text{Wi}^{-1}(\mathbf{I} - \mathbf{S}) = 0. \tag{16}$$

Here the conformation tensor $\mathbf{C}$, is related to the stress tensor $\mathbf{S}$, via

$$\mathbf{S} = \frac{\mathbf{C}}{1 - \left(\text{tr}\mathbf{C}/\ell^2\right)}, \tag{17}$$

where ℓ^2 is the parameter to enforce maximum extension of polymer coils. We use initial data for the conformation tensor from a Stokes-Oldroyd-B solution for Wi = 12 at a time that is beyond the second temporal transition when the flow is well into the periodic regime. We run a simulation of FENE-P from this initial data for $t = 1600$ time units with diffusion set to $\nu_p \approx 0.0006$, and a length cut off $\ell^2 = 400$. After this flow reaches a new near-periodic state we set the diffusion to zero and continue the simulations. A POD of the data for this simulation of FENE-P at Wi = 12 is performed and we find the behavior to be strikingly similar to the Wi = 10 case for Stokes-Oldroyd-B explained in Section 3.3.1. In particular we need 10 modes to capture 95%$\mathbf{E}_{\text{ve}}$ and the first 3 modes capture 78%$\mathbf{E}_{\text{ve}}$, (compared to 76%$\mathbf{E}_{\text{ve}}$ for Wi = 10, Oldroyd-B) with the second and third mode in pairs. The period of the highest energy mode is approximately $T_{\text{mode 1}} = 250$. We show the first 4 temporal coefficients of the POD over $5T_{\text{mode 1}}$ for FENE-P at Wi = 12 in Fig. 20 (a) to make a comparison with the temporal structure of the solution for Oldroyd-B at Wi = 10, plotted in Fig. 20 (b).

6. Conclusion

We have analyzed the dynamics for the Stokes-Oldroyd-B system of a viscoelastic fluid at zero Reynolds number in a 2D periodic geometry with a 4-roll mill background force. The system demonstrates multiple bifurcations and an underlying complex dynamical system. As the Weissenberg number is increased, in the range $4 \le \text{Wi} \le 12$, the system transits from steady solutions to periodic solutions to aperiodic solutions and back again to periodic solutions. Some of these dynamics are complicated, and we have used POD to examine them. We define an energy based on the square-root of the conformation tensor to perform the POD in terms of the elastic energy of the system. This technique has previously only been used to examine high Reynolds number elastic turbulence.

The POD gives a low mode representation to the system which is connected to essential dynamics of the flow, and easily demonstrate transitions in the flow. We have found that we need at most 14 modes to capture 95% of the energy of the system using the POD, which is a fairly small set of modes. Furthermore, in our examples we have shown that the POD is able to capture both the long-time dynamics of the system or the transients from different solution types depending on what time-series of data is used in the decomposition. Either representation may be useful depending on the application.

Another advantage of using a POD is the ability to approximate the temporal behavior of the flow with only a few time-independent geometric modes and scalar temporal coefficients or modes. This small set

of spatial and temporal modes replaces numerous snapshots, and still is able to capture the flow dynamics with reasonable accuracy. We found that we could reconstruct the time evolution of tr$\mathbf{S}$ with $\approx 10\%$ relative error in space and time (except for Wi = 8). Using the POD as an approximation provides a significant savings in data storage. The true benefit of the compression capability of the POD would be seen for 3D simulations or simulations with very long channel flow geometries. These more computationally expensive geometries are where physical purely elastic instabilities have been experimentally measured [15,54], and the POD provides a new way to analyze the dynamics in these geometries.

Acknowledgment

This work was supported by US NSF-DMS 1664679.

Supplementary material

Supplementary material associated with this article can be found, in the online version, at doi:10.1016/j.jnnfm.2018.12.009.

References

[1] E.S.S.J. Muller, R.G. Larson, A purely elastic transition in Taylor-Couette flow, Rheol. Acta 28 (1989) 499.
[2] G.H. McKinley, J.A. Byars, R.A. Brown, R.C. Armstrong, Observations on the elastic instability in cone-and-plate and parallel-plate flows of a polyisobutylene Boger fluid, J. Non-Newton. Fluid Mech. 40 (1991) 201.
[3] A. Oztekin, R.A. Brown, Instability of a viscoelastic fluid between rotating parallel disks: analysis for the Oldroyd-B fluid, J. Fluid Mech. 255 (1993) 473.
[4] J.A. Byars, A. Öztekin, R.A. Brown, G.H. McKinley, Spiral instabilities in the flow of highly elastic fluids between rotating parallel disks, J. Fluid Mech. 271 (1994) 173.
[5] P. Pakdel, G.H. McKinley, Elastic instability and curved streamlines, Phys. Rev. Lett. 77 (12) (1996) 2459–2462, doi:10.1103/PhysRevLett.77.2459.
[6] E. Shaqfeh, Purely elastic instabilities in viscometric flows, Annu. Rev. Fluid Mech. 28 (1996) 129.
[7] G.H. McKinley, T. Sridhar, Filament-stretching rheometry of complex fluids, Annu. Rev. Fluid Mech. 34 (2002) 375.
[8] R.G. Owens, T.N. Phillips, Computational Rheology, 14, World Scientific, 2002.
[9] P.E. Arratia, C. Thomas, J. Diorio, J.P. Gollub, Elastic instabilities of polymer solutions in cross-channel flow, Phys. Rev. Lett. 96 (14) (2006) 144502.
[10] A.N. Morozov, W. van Saarloos, An introductory essay on subcritical instabilities and the transition to turbulence in visco-elastic parallel shear flows, Phys. Rep. 447 (3–6) (2007) 112–143.
[11] J.J. Magda, R.G. Larson, A transition occurring in ideal elastic liquids during shear flow, J. Non-Newton. Fluid Mech. 30 (1988) 1.
[12] N. Phan-Thien, Coaxial-disk flow of and Oldroyd-B fluid: Exact solution and stability, J. Non-Newton. Fluid Mech. 13 (1983) 325.
[13] A. Groisman, V. Steinberg, Elastic turbulence in a polymer solution flow, Nature 405 (6782) (2000) 53.
[14] A. Groisman, V. Steinberg, Elastic turbulence in curvilinear flows of polymer solutions, New J. Phys. 6 (1) (2004) 29.
[15] L. Pan, A. Morozov, C. Wagner, P. Arratia, Nonlinear elastic instability in channel flows at low Reynolds numbers, Phys. Rev. Lett. 110 (17) (2013) 174502.
[16] N. Burshtein, K. Zografos, A.Q. Shen, R.J. Poole, S.J. Haward, Inertioelastic flow instability at a stagnation point, Phys. Rev. X 7 (4) (2017) 041039.
[17] P. Sousa, F. Pinho, M. Alves, Purely-elastic flow instabilities and elastic turbulence in microfluidic cross-slot devices, Soft Matter 14 (8) (2018) 1344–1354.
[18] G. Boffetta, A. Celani, A. Mazzino, A. Puliafito, M. Vergassola, The viscoelastic Kolmogorov flow: eddy viscosity and linear stability, J. Fluid Mech. 523 (2005) 161–170.
[19] B. Thomases, M. Shelley, Emergence of singular structures in Oldroyd-B fluids, Phys. fluids 19 (10) (2007) 103103.
[20] R. Poole, M. Alves, P. Oliveira, Purely elastic flow asymmetries, Phys. Rev. Lett. 99 (16) (2007) 164503.
[21] S. Berti, A. Bistagnino, G. Boffetta, A. Celani, S. Musacchio, Two-dimensional elastic turbulence, Phys. Rev. E 77 (5) (2008) 055306.
[22] L. Xi, M.D. Graham, A mechanism for oscillatory instability in viscoelastic cross-slot flow, J. Fluid Mech. 622 (2009) 145–165.
[23] B. Thomases, M. Shelley, Transition to mixing and oscillations in a Stokesian viscoelastic flow, Phys. Rev. Lett. 103 (9) (2009) 094501.
[24] B. Thomases, M. Shelley, J.-L. Thiffeault, A Stokesian viscoelastic flow: transition to oscillations and mixing, Physica D 240 (20) (2011) 1602–1614.
[25] J. Zilz, R. Poole, M. Alves, D. Bartolo, B. Levaché, A. Lindner, Geometric scaling of a purely elastic flow instability in serpentine channels, J. Fluid Mech. 712 (2012) 203–218.
[26] A. Fouxon, V. Lebedev, Spectra of turbulence in dilute polymer solutions, Phys. Fluids 15 (7) (2003) 2060–2072.
[27] A.N. Morozov, W. van Saarloos, Subcritical finite-amplitude solutions for plane Couette flow of viscoelastic fluids, Phys. Rev. Lett. 95 (2) (2005) 024501.
[28] B. Liu, M. Shelley, J. Zhang, Oscillations of a layer of viscoelastic fluid under steady forcing, J. Nonnewton. Fluid Mech. 175 (2012) 38–43.
[29] E.A. Isaacson, Some Periodic Solutions of the Two-Dimensional Stokes-Oldroyd-B System with Stress Diffusion, UC Berkeley, 2012 Ph.D. thesis.
[30] G. Berkooz, P. Holmes, J.L. Lumley, The proper orthogonal decomposition in the analysis of turbulent flows, Annu. Rev. Fluid Mech. 25 (1) (1993) 539–575.
[31] P.J. Schmid, D.S. Henningson, Stability and Transition in Shear Flows, 142, Springer Science & Business Media, 2012.
[32] V. Theofilis, Global linear instability, Annu. Rev. Fluid Mech. 43 (2011) 319–352.
[33] P. Holmes, J.L. Lumley, G. Berkooz, C.W. Rowley, Turbulence, Coherent Structures, Dynamical Systems and Symmetry, Cambridge University Press, 2012.
[34] J.N. Kutz, Data-driven Modeling & Scientific Computation: Methods for Complex Systems & Big Data, Oxford University Press, 2013.
[35] J.N. Kutz, S.L. Brunton, B.W. Brunton, J.L. Proctor, Dynamic Mode Decomposition: Data-driven Modeling of Complex Systems, 149, SIAM, 2016.
[36] C.W. Rowley, S.T. Dawson, Model reduction for flow analysis and control, Annu. Rev. Fluid Mech. 49 (2017) 387–417.
[37] K. Taira, S.L. Brunton, S.T. Dawson, C.W. Rowley, T. Colonius, B.J. McKeon, O.T. Schmidt, S. Gordeyev, V. Theofilis, L.S. Ukeiley, Modal analysis of fluid flows: an overview, Aiaa J. (2017) 4013–4041.
[38] S.-N. Wang, M.D. Graham, F.J. Hahn, L. Xi, Time-series and extended Karhunen-Loève analysis of turbulent drag reduction in polymer solutions, AIChE J. 60 (4) (2014) 1460–1475.
[39] C.R. Doering, B. Eckhardt, J. Schumacher, Failure of energy stability in Oldroyd-b fluids at arbitrarily low Reynolds numbers, J. Nonnewton. Fluid. Mech. 135 (2–3) (2006) 92–96.
[40] I. Hameduddin, C. Meneveau, T.A. Zaki, D.F. Gayme, Geometric decomposition of the conformation tensor in viscoelastic turbulence, J. Fluid Mech. 842 (2018) 395–427.
[41] R.B. Bird, R.C. Armstrong, O. Hassager, C.F. Curtiss, Dynamics of Polymeric Liquids, 1, Wiley New York, 1977.
[42] J. Rallison, E. Hinch, Do we understand the physics in the constitutive equation? J. Nonnewton. Fluid Mech. 29 (1988) 37–55.
[43] M. Renardy, A comment on smoothness of viscoelastic stresses, J. Nonnewton. Fluid Mech. 138 (2) (2006) 204–205.
[44] B. Thomases, An analysis of the effect of stress diffusion on the dynamics of creeping viscoelastic flow, J. Nonnewton. Fluid Mech. 166 (21) (2011) 1221–1228.
[45] P. Constantin, M. Kliegl, Note on global regularity for two-dimensional oldroyd-b fluids with diffusive stress, Arch. Ration. Mech. Anal. (2012) 1–16.
[46] N. Balci, B. Thomases, M. Renardy, C.R. Doering, Symmetric factorization of the conformation tensor in viscoelastic fluid models, J. Nonnewton. Fluid Mech. 166 (11) (2011) 546–553.
[47] J.A. Biello, B. Thomases, Equilibrium circulation and stress distribution in viscoelastic creeping flow, J. Nonnewton. Fluid Mech. 229 (2016) 101–111.
[48] A. Gupta, D. Vincenzi, Effect of polymer-stress diffusion in the numerical simulation of elastic turbulence, arXiv:1809.09648 (2018).
[49] R. Bird, P. Dotson, N. Johnson, Polymer solution rheology based on a finitely extensible bead–spring chain model, J. Nonnewton. Fluid Mech. 7 (2–3) (1980) 213–235.
[50] M. Herrchen, H.C. Öttinger, A detailed comparison of various Fene Dumbbell models, J. Nonnewton. Fluid Mech. 68 (1) (1997) 17–42.
[51] H. Giesekus, Die simultane translations-und rotationsbewegung Einer Kugel in Einer Elastoviskosen Flüssigkeit, Rheol. Acta 3 (1) (1963) 59–71.
[52] N.P. Thien, R.I. Tanner, A new constitutive equation derived from network theory, J. Nonnewton. Fluid. Mech. 2 (4) (1977) 353–365.
[53] R.D. Guy, B. Thomases, Computational Challenges for Simulating Strongly Elastic Flows in Biology, in: Complex fluids in biological systems, Springer, 2015, pp. 359–397.
[54] B. Qin, P.E. Arratia, Characterizing elastic turbulence in channel flows at low reynolds number, Phys. Rev. Fluids 2 (8) (2017) 083302.